4. THE CROSS-SECTION RATIO OF DEUTERIUM TO HYDROGEN

4.1 Introduction

The measurement of the cross-section ratio for deep inelastic scattering on deuterium to hydrogen can provide interesting information on the quark-gluon structure of nucleons. More specifically, the following issues can be addressed:

- From the ratio of the measured cross sections, σ^d/σ^p, the ratio of the structure function F_2 of the neutron to that of the proton F_2^n/F_2^p can be extracted (eq. 2.33). In the quark-parton model (sect. 2.4) of the nucleon F_2^n/F_2^p represents the ratio of the parton distributions in the neutron and the proton. Deviations of this ratio from unity are related to differences between the up and the down quark distributions in the nucleon. The region at high x is particularly interesting as in that region the valence quarks dominate, implying that the measured ratio at $x \to 1$ provides information on the relative importance of the u and d valence quarks. In the limit $x \to 1$ different predictions for F_2^n/F_2^p exist. Currently the predictions [11, 12, 13, 14] range from $\frac{1}{4}$ to $\frac{2}{3}$. In section 2.7 the different models providing these predictions are discussed. Furthermore, precise knowledge of the u and d quark distributions at high x is very important at collider energies, as the extraction of new physics at high Q^2 relies on this information [32]. At low x, the sea quarks are dominant and their distribution is usually assumed to be nearly identical for the proton and the neutron.

- DIS data on proton and 'neutron' targets can be used to investigate possible differences between the value of the ratio $R = \sigma_L/\sigma_T$ for the proton and the neutron. The difference is expressed in terms of $\Delta R = R^d - R^p$. Both NMC and SLAC have published measurements on ΔR [1] [2], which can be compared to new HERMES results, thus extending such data to lower x and Q^2 values. The existing data on ΔR are presented in figure 4.1 showing that there is no deviation from zero

observed in the presently covered (x, Q^2) domain. Possible deviations of ΔR from zero could be of interest as they might be related to differences of the gluon distribution for the proton and the neutron [33], or higher twist effects, which are discussed in the next item. It is noted that the quality and amount of the data available is limited below $x \simeq 0.1$.

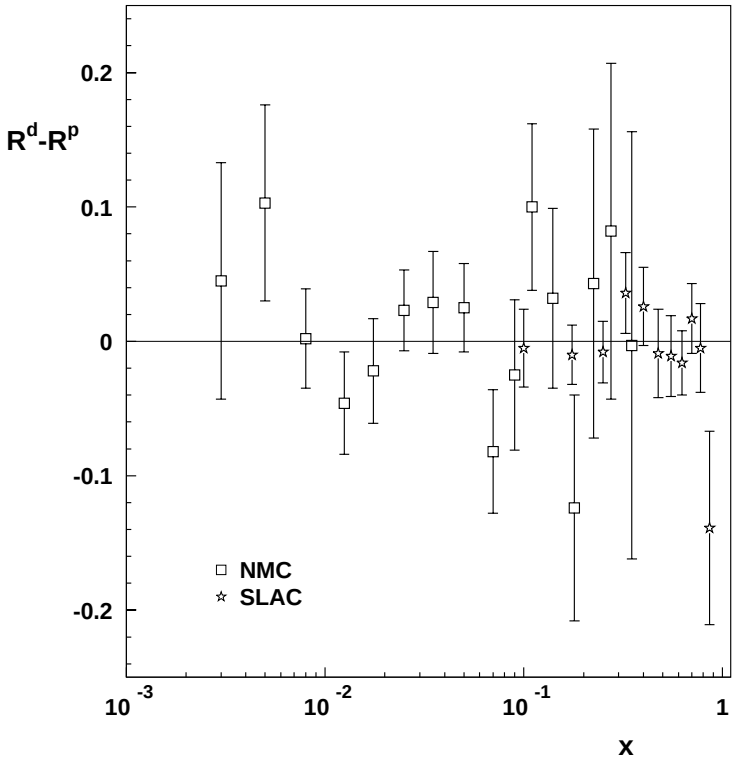

Fig. 4.1: World data on $R^d - R^p$ from NMC [1] and SLAC [2].

- Higher twist effects, which were introduced in section 2.5, can also be studied with F_2^n/F_2^p data. These effects represent quark-gluon correlations, which are possibly different for the proton and the neutron. As one does not know whether the effects are flavour dependent or possibly enhanced in the nuclear environment we study the difference between the proton and neutron (deuteron). There are two regions of interest to search for higher twist effects.

  At low x any deviation from the quark-parton-model prediction of $R = 0$ can be associated with higher twist effects. At low x also the average Q^2 is low thereby increasing the factor $1/Q^{2n}$, which governs higher twist effects, further clarifying the sensitivity for higher twist effects.

By comparing R^p and R^d in this domain it can be investigated whether in the vicinity of another nucleon these effects increase, as has been suggested [20].

At high x the differences between the quark distributions in the proton and neutron are most prominent as at high x the valence quarks dominate. Therefore, the high x region is the best domain to look for higher twist effects related to u-d quark differences. The non-perturbative phenomenological parameterisations of higher twist effects, such as the one used by Yang and Bodek [32] show this sensitivity as well: $F_2 = F_2^{pQCD}(1 + h(x)/Q^2)$ with $h(x) = a[x^b/(1-x) - c]$, i.e. the effect grows with x.

- In a recent paper [20], it has been shown how DIS data collected at HERMES can be analysed to obtain information [1] on R^A/R^d. Applying this technique to new σ^d/σ^p data, one can extract R^d/R^p, σ_L^d/σ_L^p, and σ_T^d/σ_T^p, where the subscripts, L and T, refer to the longitudinal and transverse cross section.

In this chapter the analysis of the σ^d/σ^p data is described in detail. These data are used to extract information on F_2^n/F_2^p and $R_{d/p} = R^d/R^p$ exploiting the large range of values of the virtual photon polarisation parameter, ϵ, covered by the HERMES experiment. The extraction of the ratio $R_{d/p}$ presented here[2] is not based on the Rosenbluth separation method which is explained in section 2.3. This method could not be used at HERA as all the data have been collected at a single beam energy of 27.5 GeV[3]. When combining the results of the present experiment with those obtained by NMC, effectively several beam energies are used.

This chapter is organised as follows. In section 4.2 the data selection is discussed, and the necessary corrections are described in section 4.3. The cross section ratio σ^d/σ^p is presented in section 4.4. A comparison with the existing data follows in section 4.5. The extraction of R and F_2 is the subject of section 4.6. In the subsequent section the data are used to search for higher twist effects at high x. The Gottfried sum-rule is evaluated in section 4.8. In the last section the conclusions are presented.

[1] Part of the effect reported [20] is due to an unexpected instrumental effect, i.e. photon showering in the beam pipe.

[2] This restriction only applies to those results that are based on HERMES data alone. When results are obtained from an analysis including NMC and HERMES data implicitly use is made of the Rosenbluth method.

[3] A Rosenbluth separation in the region of interest, low x and low Q^2, requires a second beam energy of a considerably higher value than the 27.5 GeV available at HERA.

4.2 Data selection

For the analysis presented in this chapter all the unpolarised hydrogen and deuterium data taken during HERMES run I (1995-2000) have been considered. In the following subsections the data selection criteria are presented as they are applied at the various levels. Also the kinematic requirements posed to identify DIS events are listed.

4.2.1 Burst selection

The runs which can be used for data analysis are selected using logs filed during data taking. In this manner unpolarised runs for hydrogen and deuterium can be identified. Every run consists of a number of bursts, for which the following data quality requirements were imposed.

- Live time : $\tau_{\text{live}} > 80\%$;
- Burst length : $9 < T_{\text{burst}} < 11$ s;
- Burst : first and last of each run are removed;
- Data-acquisition system: no error flags;
- Gain-Monitoring System : no error flags;
- Transition Radiation Detector: both top and bottom ok;
- Tracking detectors: no high voltage trips.

4.2.2 Event selection

The selection of DIS events is performed by putting requirements on several detector related quantities and by imposing certain kinematic restrictions. Concerning the kinematic requirements, two regions are distinguished: the DIS region characterised by $W^2 > 4$ GeV^2 and the baryon-resonance domain ($W^2 < 4$ GeV^2). Usually the latter domain is excluded in analyses of $F_2(x)$, but recently it has been shown [34] that for $Q^2 > 2$ GeV^2 the resonance region - on average - can be described by $F_2(x)$ derived from DIS data [35]. For that reason the data at $W^2 < 4$ GeV^2 are also considered and are referred to as "duality region" in reference to the concept of quark-hadron duality underlying this equivalence [35]. Below the requirements for valid DIS events are listed.

- Detector acceptance

- Horizontal acceptance $-170 < \theta_x < 170$ mrad
- Vertical acceptance $35 < |\theta_y| < 140$ mrad

- Target gas volume
  - Longitudinal size $-18 < z_{\text{vert}} < 18$ cm
  - Transverse size $t_{vertex} < 0.43$ cm

- Particle identification
  - Lepton identification PID3 + PID5 > 2

- DIS kinematics
  - Q^2 domain $0.1 < Q^2 < 15$ GeV^2
  - Above resonance region $W^2 > 4$ GeV^2
  - Limited size of radiative correction $y < 0.85$

- Duality kinematics
  - Resonance region $W^2 < 4$ GeV^2
  - Duality region $Q^2 > 2$ GeV^2

4.2.3 Lepton identification

The identification of leptons was done using the PID scheme presented in section 3.4.3. Leptons are identified by requiring PID3+PID5 > 2. For the data collected after 1997 PID3 reduces to PID2 as the threshold Čerenkov was replaced by a RICH, for which a separate PID scheme is used. The resulting lepton identification efficiency is 97% with a hadron contamination of only 0.01%. These numbers were obtained from a similar analysis [36].

4.2.4 Selected DIS events

After applying the selection requirements as listed above a total of about 25 million DIS events on hydrogen and deuterium were selected for analysis. The number of events per year and per gas are listed in table 4.1. As in 1999 no hydrogen data were taken, and hence no deuterium to hydrogen ratio could be determined, it was decided to add the deuterium data of 1999 to those of 2000 as there was no change in the detector system between these two periods of data taking.

Year	$H(\times 10^6)$	$D(\times 10^6)$
1996	1.71	2.83
1997	2.01	3.06
1998	0.82	1.59
1999	-	0.43
2000	10.11	2.37
total	14.66	10.30

Tab. 4.1: Number of unpolarised DIS events obtained per year during HERMES run I.

4.3 Corrections

Several corrections have to be applied to the raw data in order to be able to extract relative cross sections. The relevant corrections are described briefly below. In some cases it is argued that a given correction can be neglected for the unpolarised deuterium and hydrogen data presented in this thesis.

4.3.1 Flux factors

In order to correct the PID scheme for the non-uniformity of the flux of particles incident on the detector so-called flux factors have been introduced (see section 3.4.3). They depend on the scattering angle of the particle and its momentum. In principle, one can determine and subsequently apply these flux factors for each year and each target gas separately. However, it has been shown that for a given year the flux factors are identical if hydrogen or deuterium is used as target gas [37]. As a result the application of flux factors in the lepton identification will yield a similar change in the lepton identification efficiency and hadron contamination for both targets. Therefore, the influence of the flux factors cancels in the cross section ratio and could thus be omitted in the present analysis. To account for a possible systematic effect due to neglected flux-factor differences between hydrogen and deuterium, it has been estimated that an additional systematic uncertainty of only 0.5% needs to be introduced to the ratio of the cross sections.

4.3.2 Smearing

Partial energy losses and local inefficiencies in detector planes can cause a shift in the measured values of the kinematic variables as compared to the original values at the interaction point. To understand these shifts Monte Carlo simulations have been performed for both hydrogen and deuterium.

These simulations were carried out by M.Vincter to investigate the effect of the detector and the track reconstruction algorithm on the evaluation of the kinematic variables [38]. For the variable x a broadening of the distribution and a tail towards lower x is observed. This effect is negligible at low x, but significant at high x. In the simulation the shift of the mean to lower x and the misidentification of events at higher x have been combined, making use of a realistic cross-section parameterisation. However, since these effects are the same for hydrogen and deuterium within 0.25% these effects can be neglected as the ratio is taken. Hence, it has been decided to neglect the smearing contribution and introduce a separate contribution of 0.25% to the total systematic uncertainty on σ^d/σ^p to account for the fact that these effects were neglected.

4.3.3 Radiative corrections

The cross section ratios presented in this chapter are extracted from normalised yields of DIS events on deuterium and hydrogen. In the normalised yields events enter which do not correspond to deep inelastic scattering events. Apart from the Born cross section, which we wish to measure, there are also contributions from elastic or quasi-elastic scattering processes. These events are identified as DIS events because a photon was radiated by the scattering lepton before or after an elastic or quasi-elastic event. It may also happen that a photon is emitted by the lepton after a normal DIS event, causing a shift in the kinematics of the event. To extract the Born cross section from the data radiative corrections are applied, which correct for all these effects. The radiative corrections are calculated using the TERAD program [39]. The program takes into account the following higher order QED processes that result in the emission of additional photons: contributions from vacuum loops of all leptons and quarks, lepton pair production, electroweak interference and bremsstrahlung of one or two photons. The complete list of diagrams can be found in reference [40]. The size of the radiative corrections is different for deuterium and hydrogen, mainly due to the elastic contribution. Furthermore, there is an uncertainty associated with this correction as the phenomenological input parameters carry uncertainties. The size of the corrections and the associated uncertainties are explicitly listed in table 4.4 in section 4.4.4.

4.3.4 Photon shower effect

When collecting DIS data from nitrogen and deuterium a deviation of the cross section ratio from existing data at $x < 0.06$ and $Q^2 < 1.5$ GeV^2 was

found [20]. As the new data were collected at a much lower beam energy than used for the existing data as obtained by NMC [41], and thus corresponding to a lower value of ϵ, a new effect was thought to be found. However, further measurements on heavier targets could not be analysed consistently until it was realised that an instrumental effect caused the discrepancy with respect to previous data. The hard Bremsstrahlung photons produced in nuclear elastic scattering have a large probability of hitting detector frames for the kinematic region where the deviation was found. These Bremsstrahlung photons are mostly emitted in three directions: along the beam, along the scattered lepton and in the direction of q. It is this last (Compton scattering) peak that caused the problem. When these events occur, extensive electro-magnetic showers are produced, creating very high multiplicities in part of the spectrometer. These events are impossible to track and are rejected for further analysis, thereby causing a significant tracking inefficiency. This effect is called the Photon Shower Effect (PSE).

The calculated radiative corrections are based on the assumption that all Bremsstrahlung events are observed and therefore the correction is overestimated. This causes the extracted Born cross section to be too low. Once this was realised Monte Carlo studies were performed, which were compared to special data productions to evaluate the size of the required PSE correction. In table 4.4 the size of both the radiative corrections (column 5 and 6) and the PSE correction are presented (column 3) As expected, the PSE correction factor is largest at low x and Q^2, where the radiative corrections are also largest. It can be seen that the PSE correction on the ratio σ^d/σ^p ranges from 4.2% at low x to less then 1% for $x > 0.035$, while beyond $x \sim 0.1$ the PSE is negligible. As the correction is based on a Monte Carlo simulation that involves the rather complicated (detector frame) geometries, we have to assign a systematic uncertainty to the PSE correction, which is presented in column 4 of table 4.4 and is highest at the lowest x, 1.4%, and drops off towards $x = 0.1$.

4.3.5 Charge symmetric background

In the HERMES experiment there are various sources of e^+e^- pairs, e.g. a π^0 decaying into a $\gamma\gamma$-pair of which one photon could produce an e^+e^- pair. The e^+ or e^- lepton, depending on the beam charge, can be misidentified as the scattered lepton from a DIS event. These events are known as Charge Symmetric Background (CSB) events. The correction for these events can be taken from an analysis of events containing a lepton of opposite charge (with respect to the beam charge). The total number of events selected this way amounts to $\sim 2\%$ of the events found in the regular DIS analysis. However,

the CSB data have a significantly different x-distribution; peaking at low x. In certain low x bins the CSB can be as large as 6%. If it is assumed that the acceptance is identical for CSB and DIS events, one can subtract the CSB events per (x, Q^2) bin, where after the radiative corrections are applied.

The number of DIS events, N_{DIS}, has been evaluated as follows from the observed number of events, N_{total}, in a given bin and the number of CSB events, N_{CSB}:

$$N_{\mathrm{DIS}}(x, Q^2) = N_{\mathrm{total}}(x, Q^2) - N_{\mathrm{CSB}}(x, Q^2). \tag{4.1}$$

These numbers of events are not yet corrected for the radiative corrections, which need to be applied. This is discussed in the following section.

4.4 Experimental data on σ^d/σ^p

In this section the determination of the actual cross section ratio σ^d/σ^p is presented. This involves a number of steps, which are discussed in separate subsections on normalisation (4.4.1), error calculation (4.4.2 and 4.4.4) and reproducibility (4.4.3).

4.4.1 Normalisation

The normalisation of the selected DIS events, corrected for the CSB as described in the previous section, is done in the following manner. The overall normalisation is performed by dividing the number of events in a given bin by the total integrated luminosity ($\mathcal{L}$) for the selected bursts, corrected for the length of these bursts (T_{burst}) and the live-time of the data acquisition system (τ_{live}) for that burst. At the same time the radiative corrections (η) are applied, which reduce (or, at high x, increment) the selected number of events N_{DIS}. The radiative correction factors take into account the fact that the radiative corrections for DIS events are different from the radiative correction for CSB events. This leads to the following yield definition:

$$Y = \frac{N_{\mathrm{DIS}} \cdot \eta}{\mathcal{L} \cdot T_{\mathrm{burst}} \cdot \tau_{\mathrm{live}}} \tag{4.2}$$

The cross section ratio σ^d/σ^p per nucleon can be obtained by also taking into consideration the double number of nucleons in deuterium with respect to hydrogen.

$$\frac{\sigma^d}{\sigma^p} = \frac{Y^d/2}{Y^p} \cdot C_{pse} \tag{4.3}$$

The correction for the photon shower effect C_{pse} is taken into account as a correction on the cross section ratio for the applicable kinematics domain. It

is emphasised that Eq. 4.2 is evaluated at the burst level. The bursts have a duration of 10 s (see section 3.4.6). In the results presented hereafter, Y^d and Y^p have been integrated over a year for each bin, where after the ratio of Eq. 4.3 is evaluated.

4.4.2 Statistical uncertainties

The statistical uncertainties on the cross section ratio have been calculated taking into account the reduction of the number of events due to radiative corrections (η). This reduction can be as large as 60% in the lowest x bin, as illustrated in table 4.4. The reduction due to the CSB events (at most 6%) is also included. As a result, for the radiative corrections a factor $1/\eta^p$, representing the radiative corrections calculated for the proton target, enters, which is deduced in [42], while for the CSB correction a subtraction of the CSB is performed. The resulting absolute uncertainty on the measured cross-section ratio is obtained as follows:

$$\delta\left(\frac{\sigma^d}{\sigma^p}\right) = \frac{\sigma^d}{\sigma^p}\sqrt{\left.\frac{N_{DIS}+N_{CSB}}{(N_{DIS}-N_{CSB})^2}\right\rfloor_d + \left.\frac{N_{DIS}+N_{CSB}}{(N_{DIS}-N_{CSB})^2}\right\rfloor_p} \cdot \frac{1}{\eta^p} \qquad (4.4)$$

It is noted that for historical reasons radiative corrections are usually treated as a multiplicative factor (η^p in eq. 4.2), which is reasonable as long as as the corrections are small. In our data the corrections are large at low x and hence it would have been more appropriate to treat them in a subtractive manner. As a result the uncertainties would have increased. The factor η^p in eq. 4.4 accounts for this enlargement of the uncertainties, while keeping to the multiplicative approach.

4.4.3 Reproducibility

In order to investigate the reproducibility of the measurements, the data taken in the years '96, '97, '98, and '99 together with 2000 have been analysed separately. As a first step we compared the present analysis of the 1996 data with an early analysis performed by Vincter[43]. In figure 4.2 the comparison is shown between the σ^d/σ^p ratio produced by both analyses. It is noted that the analyses are based on two different versions of the basic event reconstruction and have employed different data quality criteria and different kinematic requirements. In particular the W^2 and Q^2 requirements were different. In the so-called 96b3 μDSTs used by Vincter the reconstruction included the tracks recorded by the vertex chambers, while those were not used (in order to be consistent with later years) in the 96c1 μDSTs used

in the present analysis. The agreement between the two analyses is reasonable, especially if it is realised that the correction for the PSE nor the error enlargement factor $(1/\eta^p)$ were considered by Vincter. Since a different binning is used in the two analyses, no point to point comparison can be made. However, by comparing the data set from the analysis performed by M. Vincter with a fit to the data set of this analysis, similar to the fit shown in figure 4.9, an agreement was found with a confidence level of 95% in the kinematic overlap region between the two analyses. It can be seen in figure 4.2 that in the present analysis a larger kinematic range is covered. This is a consequence of the reduced restrictions on x (Vincter: $x > 0.012$) and W^2 (Vincter: $W^2 > 4$), which is related to the proof of duality.

To verify the year-to-year reproducibility, the cross section ratios are shown in figure 4.3 for each year separately. For each year the data are also divided by a fit of the sum of the data over all years in order to establish the relation of each year with respect to the five-year average. It is seen that the shapes of the cross-section ratio for the different years agree very

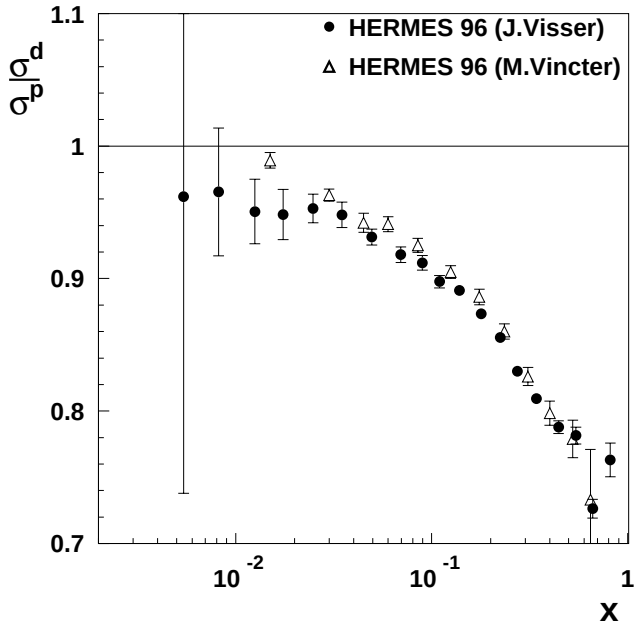

Fig. 4.2: Ratio of the cross section per nucleon for deuterium and hydrogen as a function of x. Two analyses are compared, both performed on the HERMES 1996 data sample. The open triangles represent the analysis done by M. Vincter using the 96b3 μDSTs, involving different kinematic requirements, while the solid circles show the results of the present analysis performed on the 96c1 μDSTs.

well, while the relative normalisation factors are compared in table 4.2. It is noticed that the '97 cross section ratio is $1.2 \pm 0.1\%$ low with respect to the average. This is significantly more than the deviation of the other years with respect to the average and cannot be explained as a statistical fluctuation. While searching for a cause to explain the reduced cross-section ratio of the

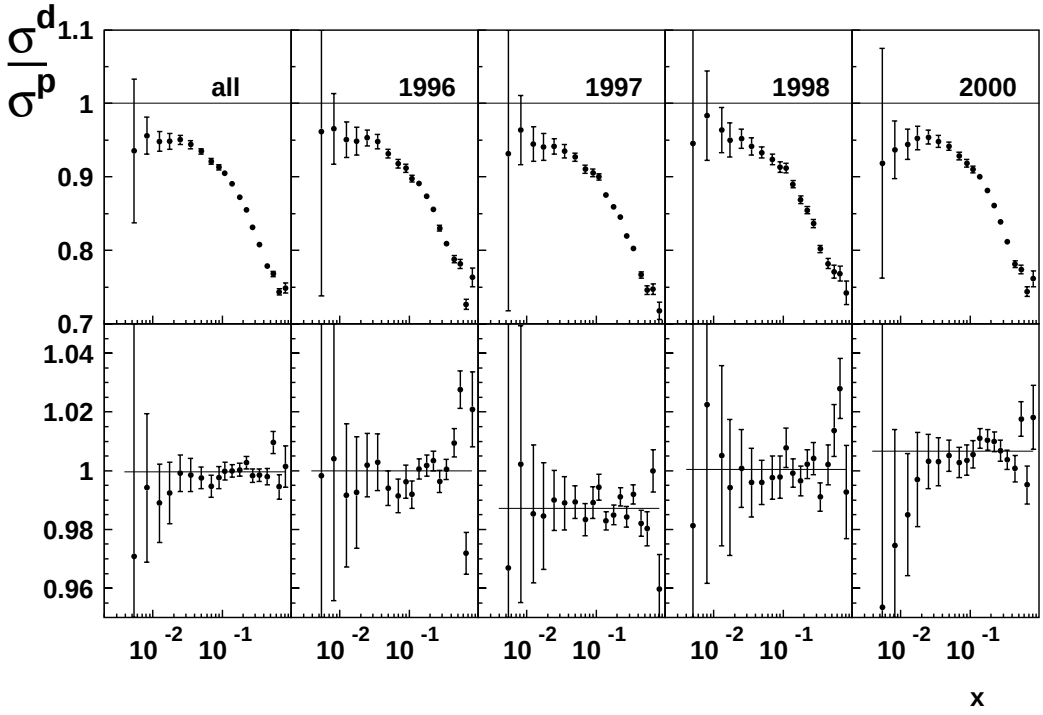

Fig. 4.3: The deuterium to proton cross-section ratio as measured in four different periods, i.e. '96, '97, '98, and '99 and 2000 combined. In the lower panel the ratio of the measured data, as presented in the upper panel, to the fit of all data combined, like the fit in figure 4.9, is shown.

'97 data a non-linear behaviour of the deuterium yield with respect to the luminosity rate was found. In order to further investigate this, all fills in which both deuterium and hydrogen data were collected, were analysed separately. Several fills showed a large (up to 10%) drop in the cross-section ratio, while in the data quality information nothing could be found to explain this drop. It is concluded that the '97 data set suffers from a non-linear behaviour of the rate as measured by the luminosity monitor, which does not show up in later years due to subsequent changes to the device. Therefore the '96, '98, and the combined '99 and 2000 data sets were added to verify the normalisation of all years with respect to the weighted average. This produced a deviation

	1996	1997	1998	1999+2000
I	0.1 ± 0.1	-1.2 ± 0.1	0.1 ± 0.2	0.7 ± 0.1
II	-0.4 ± 0.1	-1.7 ± 0.1	-0.3 ± 0.2	0.3 ± 0.1

Tab. 4.2: Relative deviation (in %) of the different years with respect to the grand total. Total I includes all years and total II excludes 1997.

of at most 0.4 ± 0.1% (for the '96 data set), while for the '97 cross section ratio a 1.7 ± 0.1% deviation was found. It was concluded that the '96, '98 and '99 and '00 data sets are in mutual agreement. As the '97 cross-section ratio is systematically low, presumably due to the non-linear luminosity monitor behaviour, it was decided to renormalise the '97 cross-section ratio by 1.7%. After the normalisation the '97 data were added to the other data sets for further analysis. The systematic uncertainty due to the spread in the measured cross-section ratios for different years can be roughly estimated by taking the statistically weighted sum of the reproducibility factors. Adding the deviations weighted by their uncertainties corresponds to a systematic uncertainty due to the limited reproducibility of the data of 0.7%.

4.4.4 Systematic uncertainties

The total systematic uncertainty on the measured cross-section ratio is given by the uncorrelated contributions, associated with particle identification, smearing corrections, the uncertainty in reproducing the cross-section ratio for different years, the uncertainty in the estimation of the photon shower effect (PSE), and the systematic uncertainty on the radiative corrections. The x and Q^2 independent contributions to the total systematic uncertainty are listed in table 4.3. They are added in quadrature to yield an uncertainty of 0.9%. The uncertainties on the photon shower effect and the radiative cor-

Contribution	Uncertainty
Flux factors	$< 0.5\%$
Smearing	$< 0.25\%$
Reproducibility	$\simeq 0.7\%$
Total	$\simeq 0.9\%$

Tab. 4.3: Overview of the x and Q^2 independent contributions to the total systematic uncertainty on the cross section ratio.

rections are clearly depending on x and Q^2 and therefore they are presented

in table 4.4, where their x dependence is shown. The size of the photon shower effect correction and the radiative corrections are listed in column 3, 5 and 6, while the contribution to the systematic uncertainties are presented in columns 4 and 7, respectively. The radiative corrections are calculated for hydrogen and deuterium separately, while the systematic uncertainties on the radiative corrections are given for the cross-section ratio. The systematic uncertainty on the PSE is presented in figure 4.4. In the upper panel the

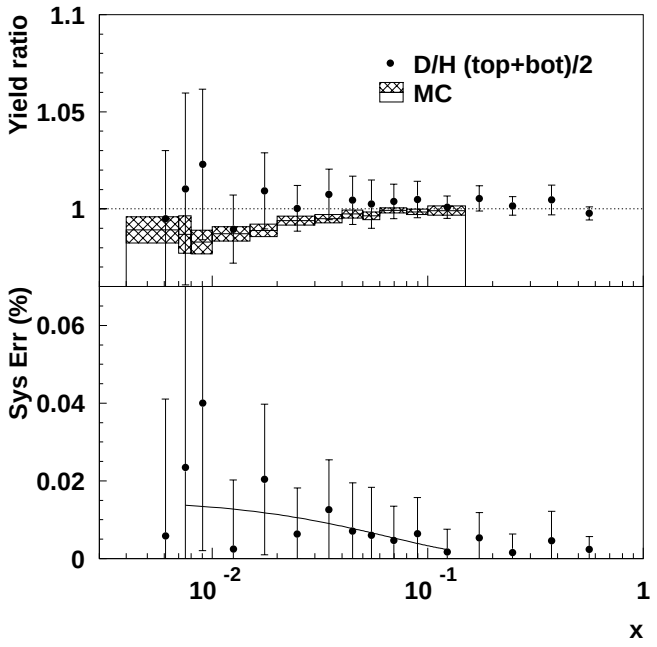

Fig. 4.4: Photon-shower-effect systematic uncertainty (lower panel), deduced from the comparison of the special data analysis and the Monte Carlo studies (upper panel).

comparison between data and Monte Carlo is shown. The data have been produced with a special tracking analysis to establish the size of the PSE. Presented is the average of the σ^d/σ^p analysis performed using only the top detector half and only the bottom part of the spectrometer. The difference between the result obtained from the data as compared to the Monte Carlo results is shown in the lower panel. The difference becomes larger at low x and somewhat unstable due to the limited data available for this study. To work with a smooth systematic uncertainty, the shown difference was fitted by a smooth 2^{nd} order polynomial. The result is plotted in the lower panel

and used to evaluate the PSE systematic uncertainty listed in table 4.4. The total uncertainty, when taking into account the other contributions, is listed in the last column of table 4.4. In this table the relative error is presented, while in the figures the systematic error band shown represents the absolute systematic uncertainty for ease of interpretation.

x	Q^2	PSE(corr)	PSE(sys)	RC(p)	RC(d)	RC(sys)	total(sys)
0.0038	0.17	0.959	0.0145	0.28	0.41	0.039	0.046
0.0053	0.23	0.958	0.0142	0.32	0.43	0.033	0.040
0.0081	0.34	0.963	0.0136	0.39	0.49	0.033	0.040
0.0125	0.49	0.963	0.0127	0.48	0.56	0.030	0.037
0.0174	0.65	0.971	0.0117	0.55	0.61	0.027	0.034
0.0248	0.86	0.985	0.0105	0.62	0.66	0.025	0.032
0.0348	1.11	0.992	0.0090	0.68	0.71	0.024	0.031
0.0495	1.40	0.995	0.0072	0.74	0.77	0.018	0.026
0.0695	1.73	0.996	0.0052	0.80	0.82	0.013	0.022
0.0896	1.98	0.997	0.0038	0.84	0.86	0.010	0.020
0.1096	2.18	1.0	0.0000	0.87	0.89	0.008	0.019
0.1388	2.42	1.0	0.0000	0.91	0.92	0.008	0.019
0.1789	2.68	1.0	0.0000	0.95	0.96	0.008	0.019
0.2234	2.92	1.0	0.0000	0.99	1.00	0.008	0.019
0.2732	3.16	1.0	0.0000	1.02	1.03	0.008	0.019
0.3418	3.75	1.0	0.0000	1.06	1.07	0.007	0.019
0.4444	4.36	1.0	0.0000	1.11	1.11	0.006	0.018
0.5441	4.45	1.0	0.0000	1.16	1.17	0.005	0.018
0.6629	4.31	1.0	0.0000	1.22	1.23	0.005	0.018
0.8163	4.05	1.0	0.0000	1.19	1.21	0.014	0.022

Tab. 4.4: Size of PSE and the radiative corrections (columns 3, 5 and 6) and their contribution to the systematic uncertainty and the total systematic uncertainty, including the contribution given in table 4.3, for the cross-section ratio for each x and Q^2 bin.

4.5 Comparison with previous measurements

In this section the HERMES data on σ^d/σ^p are compared to the data, previously collected by NMC [1] and SLAC [44]. First, the comparison will be made in the x-domain and then for each x-bin the Q^2-dependence of the data is presented.

4.5.1 Cross section ratio dependence on x

The cross-section ratio as measured at HERMES is presented in figure 4.5. In the left panel the data are compared to similar data obtained by NMC [1]. The NMC data were recorded using four different beam energies: 90, 120, 200 and 280 GeV. The kinematic range covered by the NMC data begins at $x = 0.0015$ and $Q^2 = 0.16$ GeV^2 and goes up to $x = 0.675$ and $Q^2 = 26.9$ GeV^2 corresponding to an average Q^2 of ~ 10 GeV^2 [45].

The shape of the two distributions is somewhat different. In order to investigate whether the difference in shape can be explained by the difference in average Q^2, at which the two data sets have been taken, we compare the HERMES data to a parameterisation [45] of the existing data, which is based on measurements from NMC, BCDMS, and SLAC. In this parameterisation the average Q^2 for each x bin can be inserted to evaluate σ^d/σ^p in each x bin, i.e. the parameterisation effectively includes the DGLAP evolution as described in section 2.5

This procedure leads to a better description of the data as can be seen in the upper plot in the right panel of figure 4.5, although there is a hint of possible small deviations at the extremes of the x distribution. To enhance possible differences at low and high x the HERMES data have been divided by the world data parameterisation. In the lower plot in the right panel of figure 4.5 small deviations from a flat behaviour can be observed at low and high x. Such deviations might be due to higher twist effects.

To study these differences the two kinematic regions will be considered separately in sections 4.6 and 4.7, respectively. At the highest x such an effect will correspond to a Q^2 dependence of F_2^d/F_2^p. At low x, where the Q^2 dependence is already known to be small [46], higher twist effects may show up in R, i.e. as a Q^2-dependent difference between R^d and R^p. These possible higher twist effects on R can be investigated by studying the ϵ-dependence of σ^d/σ^p. In the remainder of this chapter these deviations are studied in more detail by evaluating the Q^2-dependence of F_2^d/F_2^p at high x and the ϵ-dependence of σ^d/σ^p at low x.

4.5.2 Q^2-dependence

Comparing the HERMES data as a function of x with a Q^2-evolved parameterisation cannot reveal the details contained in the measurements. Therefore, the data are presented as a function of Q^2 in figures 4.6 and 4.7 for every x-point shown in figure 4.5. A comparison is made with both the NMC and SLAC data. The data sets agree well over most of the x and Q^2 region. However, possible small differences are hard to distinguish. To compare the

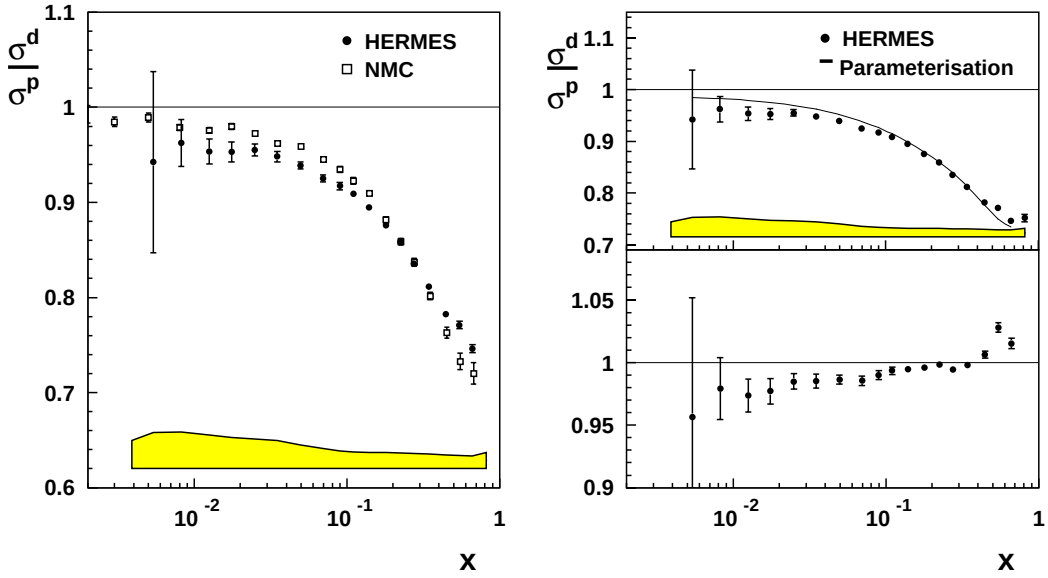

Fig. 4.5: In the left panel the comparison of σ^d/σ^p between the HERMES and NMC results is shown. The HERMES data are represented by the solid circles, the NMC data by the open squares. The error band indicates the systematic uncertainty.
The right-hand panel presents the comparison of the HERMES data with the world data parameterisation [45]. The parameterisation is calculated for the $\langle x \rangle$ and $\langle Q^2 \rangle$ values of the HERMES experiment. The lower part shows the deviation of the HERMES data from the parameterisation.

Q^2-dependence for the HERMES and NMC data sets, the following function was used to fit the data:

$$\frac{\sigma^d}{\sigma^p}(\langle x \rangle, Q^2) = a(x) + b(x) \ln Q^2 \tag{4.5}$$

The fit of the NMC data yielded the same values for a and b as were published [46]. Subsequently the same fit was used to extract a and b for the present data. A comparison for a and b obtained in this way is presented in figure 4.8. The offset a, which corresponds to σ^d/σ^p at $Q^2 = 1$, is in fair agreement for the two data sets. Remaining differences (of a few %) in the mid x-range possibly reflect a normalisation difference between the HERMES and NMC data, which is further discussed in section 4.6.2. For the slope, b, the HERMES data show a weak trend from slightly positive b-values at $x \sim 0.04$ to slightly negative b-values at high x, while the Q^2-dependence found for NMC is very small over the whole kinematic range. Assuming that

the intrinsic Q^2-dependence of the data must be the same, the possible difference between $b(x)$ for both data sets can be due to an ϵ-dependence of the cross-section ratios. This is discussed in detail in the subsequent sections. However, in view of the large uncertainties involved the differences between the HERMES and NMC data displayed in figure 4.8, need not be significant.

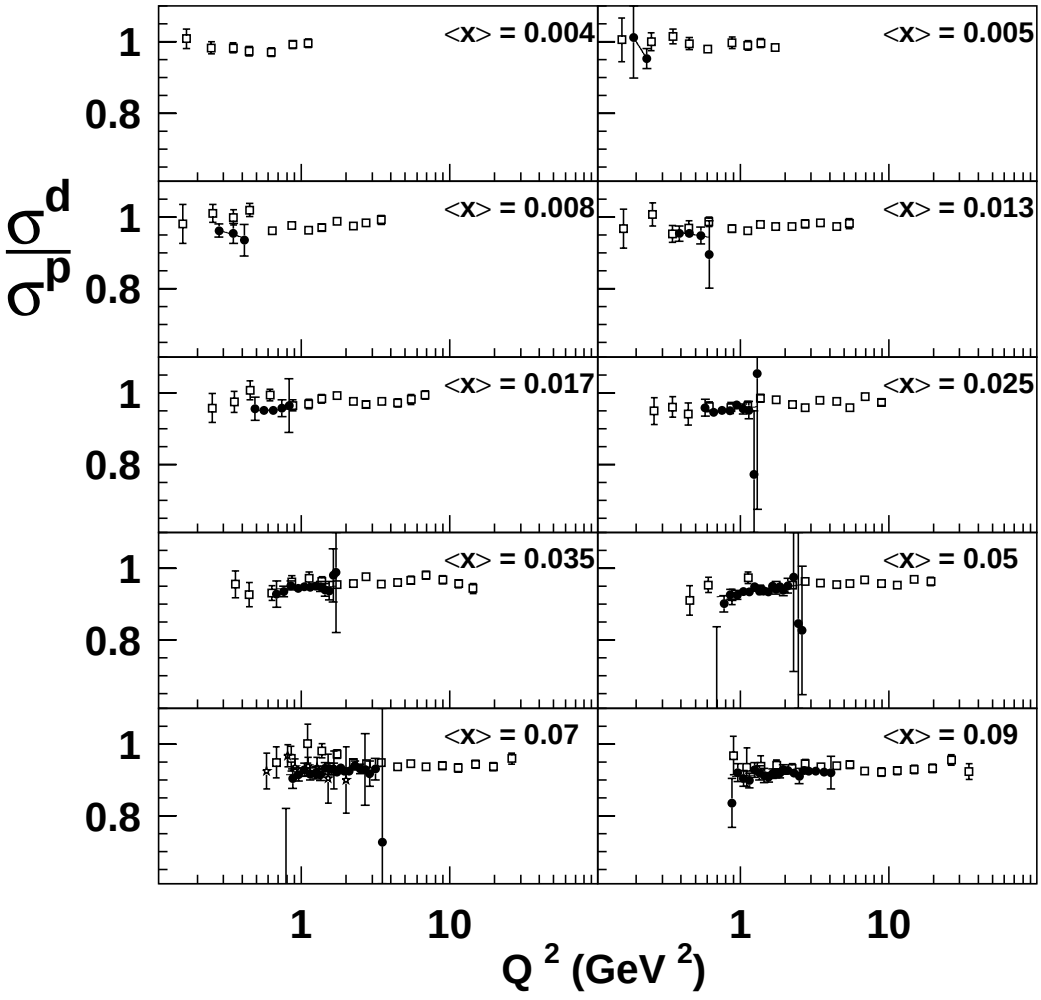

Fig. 4.6: The cross-section ratio per nucleon as a function of Q^2 in the different x regions for the HERMES (full circles), NMC (open squares), and SLAC (open stars) data. Also shown is the result of a fit as described by equation 4.5.

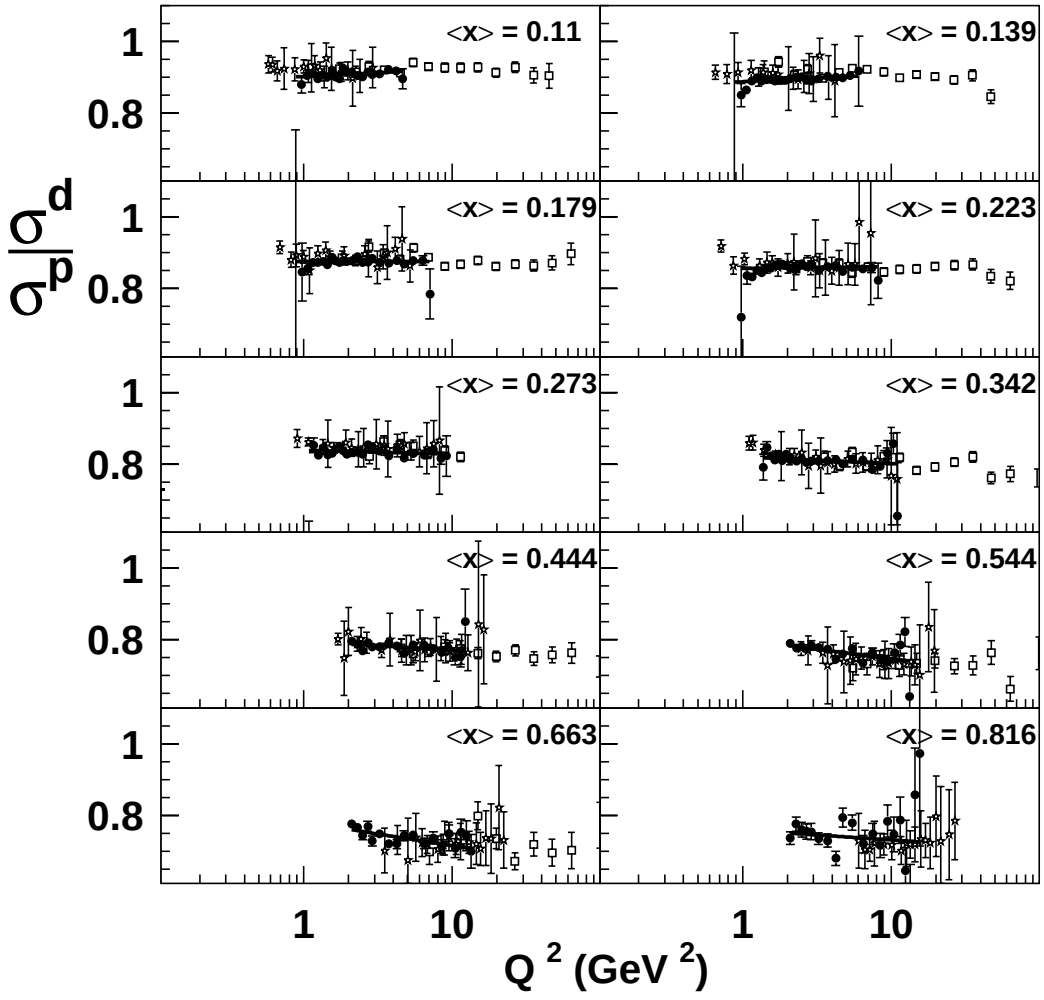

Fig. 4.7: The cross-section ratio per nucleon as a function of Q^2 in the different x regions for the HERMES (full circles), NMC (open squares), and SLAC (open stars) data. Also shown is the result of a fit as described by equation 4.5.

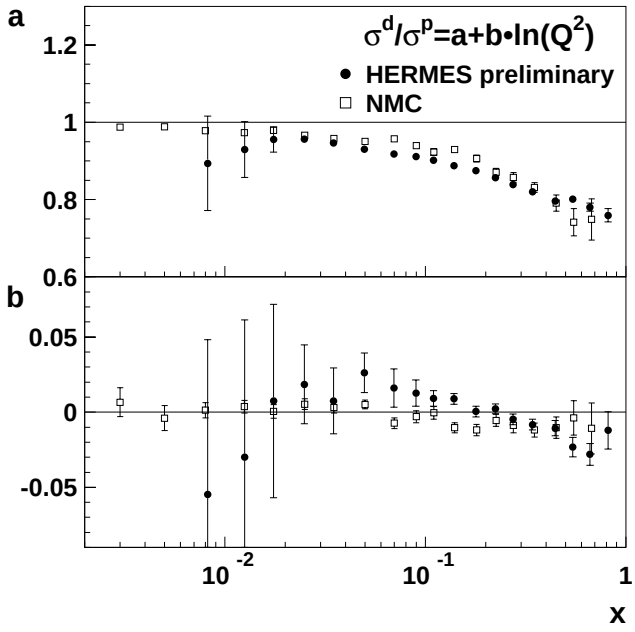

Fig. 4.8: The result of a $\ln(Q^2)$-dependent fit. The offset $a(x)$ (upper panel) and the slope $b(x)$ (lower panel) are shown for both the HERMES data (solid circles) and the NMC data (open squares). Note that the systematic uncertainties (typically a few % in each data set) are not displayed.

4.6 Extraction of R and F_2 related quantities

In order to extract R and other related quantities from the data a fitting procedure is adopted. The cross-section ratios are plotted versus ϵ for each x-bin. By fitting these data with two free parameters several quantities can be extracted, as will be explained in this section. However, before these fits can be performed several corrections have to be applied to the data, which will be dealt with first.

4.6.1 Bin-centring correction

The fitting of the ϵ-dependence at fixed x is not straightforward as the data contained in a certain x-bin are collected at slightly different x-values. Therefore, a bin-centring correction is needed such that all data are made to correspond with the weighted average $\langle x \rangle$ of that bin. For this bin-centring correction the cross-section ratio versus x was fitted with the following functional form:

$$f_{d/p}(x) = a + bx + cx^2 + dx^3 + e \ln x \tag{4.6}$$

The resulting curve[4] is shown in figure 4.9 together with the data, which are well described. Subsequently, the fit was used to correct the measured cross-

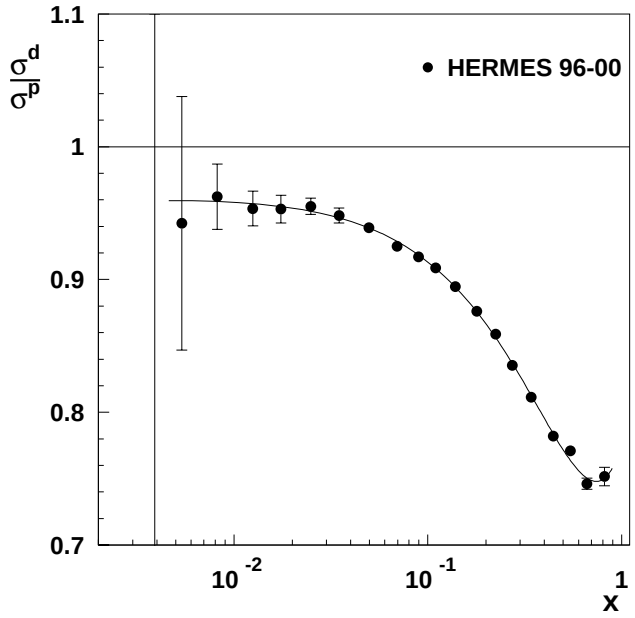

Fig. 4.9: Fit to the deuterium to proton cross-section ratio using the functional form given by equation 4.6.

section ratio within each x-bin applying the following procedure to each data point contained in that x-bin:

$$\frac{\sigma^d}{\sigma^p}(\langle x\rangle, Q^2, \epsilon) = \frac{\sigma^d}{\sigma^p}(x, Q^2, \epsilon) \cdot \frac{f_{d/p}(\langle x\rangle)}{f_{d/p}(x)}, \tag{4.7}$$

where x corresponds to the measured value and $\langle x\rangle$ to the weighted average of x in the selected x-bin. The size of the correction is less than 0.1%.

4.6.2 Relative normalisation of the NMC and HERMES data

In order to verify the relative normalisation of the NMC and HERMES data, the measured values of σ^d/σ^p have been compared for each x-bin, using the combined representation of the data as shown in figures 4.6 and 4.7, with the requirement that the measured Q^2 values from NMC do not deviate from the HERMES Q^2 values by more than 10%. The comparison has only been made

[4] The fitting parameters obtained have the following values; $a = 0.96$, $b = -0.54$, $c = 0.30$, $d = 0.07$, $e = -0.004$

if for both data sets ϵ is larger than 0.8, otherwise the relative normalisation could be biased by a possible ϵ-dependence of the data.

For all data satisfying the aforementioned requirements the weighted average of σ^d/σ^p in the overlap region was calculated for both HERMES and NMC. These numbers were divided and fitted by a constant, the result is shown in figure 4.10. The data at lowest $x(< 0.02)$ and highest $x(> 0.4)$

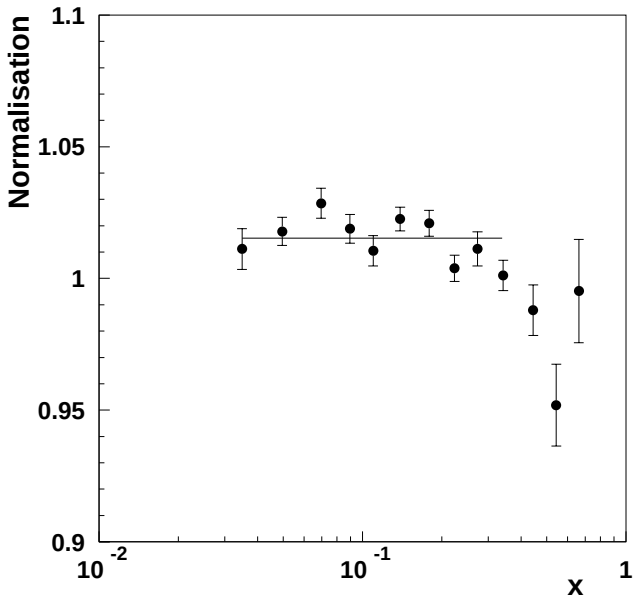

Fig. 4.10: Normalisation with respect to NMC data versus x in the overlap region in $Q^2$and for $\epsilon > 0.8$.

were excluded from the fit due to a lack of overlap in ϵ (at low x) and to exclude the region where higher twist effects could occur (at large x). The obtained value for this constant is 1.017 ± 0.001. As can be seen from figure 4.10, the data at high x are systematically below the average, giving a first hint for possible higher twist effects.

Considering the small systematic uncertainty of the NMC data (0.5%) as compared to the HERMES systematic uncertainty of, on average, 2.0%, it was chosen to re-normalise the HERMES data by 1.7%. In this way both data sets are now combined in order to study the ϵ-dependence of the data. The main advantage of using both data sets in this investigation is the increased coverage in ϵ, especially at low x. Effectively, the analysis resembles a Rosenbluth separation because we make use of basically five data sets, as the NMC data have been collected at four different beam energies. The five data sets together cover beam energies from 27.5 GeV to 280 GeV.

4.6.3 Extraction of R^d/R^p and F_2^d/F_2^p

The ϵ-dependence can be used to extract information on R^d/R^p and F_2^d/F_2^p, using the following relation to fit the data.

$$\frac{\sigma^d}{\sigma^p}(\epsilon) = \frac{F_2^d}{F_2^p} \cdot \frac{(1+\epsilon k(x,Q^2)R^p)(1+R^p)}{(1+k(x,Q^2)R^p)(1+\epsilon R^p)} \quad , \tag{4.8}$$

From this equation it can be seen that the intersection of the fit at $\epsilon = 1$ yields a value for F_2^d/F_2^p, while the slope is a measure for $k(x,Q^2) = R^d/R^p$. In the fit two free parameters are used: F_2^d/F_2^p and $k(x,Q^2)$. For R^p the R1990 [47] parameterisation was used. This parameterisation is shown in figure 4.11. The ϵ-dependence of the bin-centred and renormalised HERMES data are

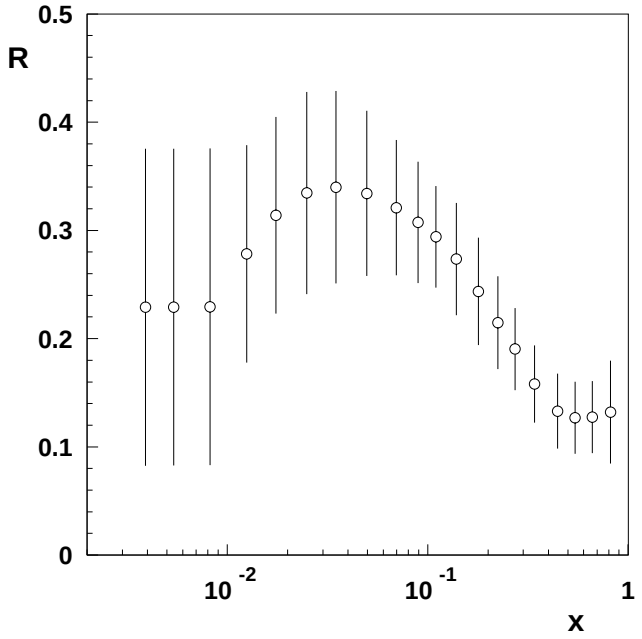

Fig. 4.11: The values of R from the R1990 parameterisation [47] evaluated at x and Q^2 values corresponding to those of the present experiment. The error bars represent the uncertainty of the parameterisation.

presented in figures 4.12 and 4.13 together with the NMC data obtained in the same (x,Q^2) range. The resulting fits obtained based on the fit to the data using equation 4.8 are shown as well. All these data were already shown in figure 4.6 and 4.7, but in this case fewer NMC data are displayed due to the required similarity in Q^2.

In the left panel of figure 4.14 the resulting F_2^d/F_2^p values are plotted versus x together with the σ^d/σ^p values, as measured directly. It is noted

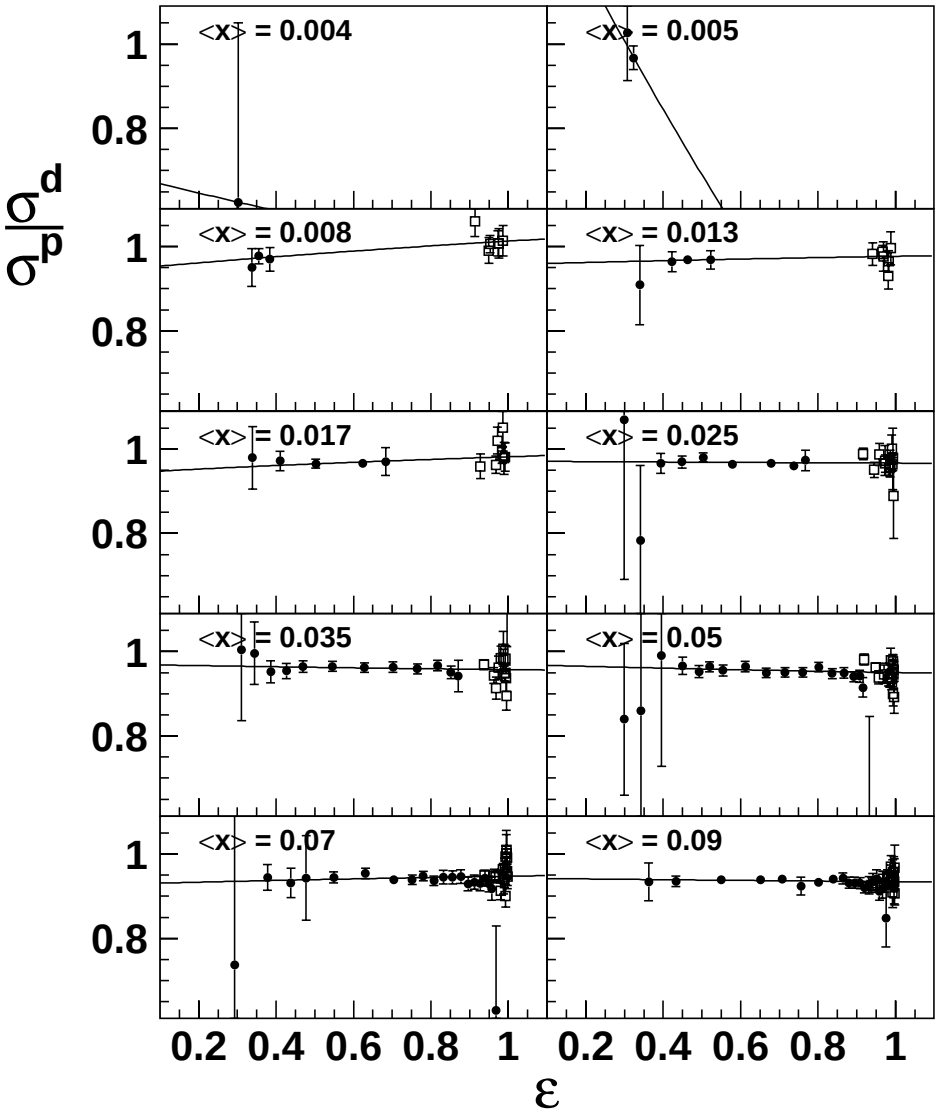

Fig. 4.12: DIS cross-section ratio per nucleon for deuterium to proton as a function of ϵ. Presented are the HERMES data (full circles) and the NMC data (open squares), which were collected at similar Q^2 values. Also shown is the fit as obtained using eq. 4.8.

that the uncertainty in the fit is very large for the first three x-bins due to the statistical uncertainty of the data. For that reason they are not shown in figure 4.14. For similar reasons no results are shown for $x > 0.4$ in the right panel of figure 4.14. In this case the short lever arm in ϵ induces large uncertainties in the fit. The upper systematic error band indicates the absolute

systematic uncertainty on the direct measurement, while the lower error band represents the uncertainty on the result from the fit. The determination of the systematic errors is discussed in detail in the next section. The fact that the systematic uncertainty of the direct measurement is larger than the one of the result from the fitting procedure can be understood as follows. The direct measurement is based on HERMES data only, while the result from the fit is in addition based on the NMC data. For the extraction of F_2^d/F_2^p the NMC data dominate the result of the fit, as the NMC data are taken at high ϵ and the values of the fit at $\epsilon = 1$ determine the values of F_2^d/F_2^p. This is clear from equation 4.8. The size of the systematic uncertainty for these NMC data is very small and therefore the resulting systematic uncertainty is small. The values of F_2^d/F_2^p as determined by the two different methods are very close. Only at low x deviations can be observed due to the limitations of the fitting procedure. The similarity of the two determinations of F_2^d/F_2^p implies that $R^d \sim R^p$, which is confirmed by the results of the fit for R^d/R^p. In the right-hand panel of figure 4.14 the fitted values of R^d/R^p are presented versus x. The fact that no deviation from 1 is observed for R^d/R^p, which implies that the value for R^d does not differ from R^p, is consistent with earlier measurements. However, the present measurements extend this observation to lower values of x and Q^2 (see section 4.6.5).

4.6.4 Systematic uncertainties

The systematic uncertainties on the measured cross-section ratio have already been discussed in section 4.4.4. Here, we focus on the systematic uncertainties of the results obtained by the fitting procedure. Two independent sources can be recognised: the systematic uncertainty on the measured cross-section ratio; or more specifically to what degree the results from the fit can vary when the data points are shifted up or down with this uncertainty. Secondly, the uncertainty on the chosen parameterisation of R^p, which is presented in figure 4.11.

As the NMC data are used in the fitting procedure the question arises in what manner the systematic uncertainty on these data have to be taken into account. The main contribution to the NMC systematic uncertainty is the uncertainty in the radiative corrections, which have been calculated with the same program as used at HERMES. Therefore, when moving the HERMES data points up and down with their systematic uncertainty, the NMC data are moved in the same direction with their systematic uncertainty. By comparing the two values, obtained in this way, with the central values from the fits the final systematic uncertainty is evaluated by averaging the two differences.

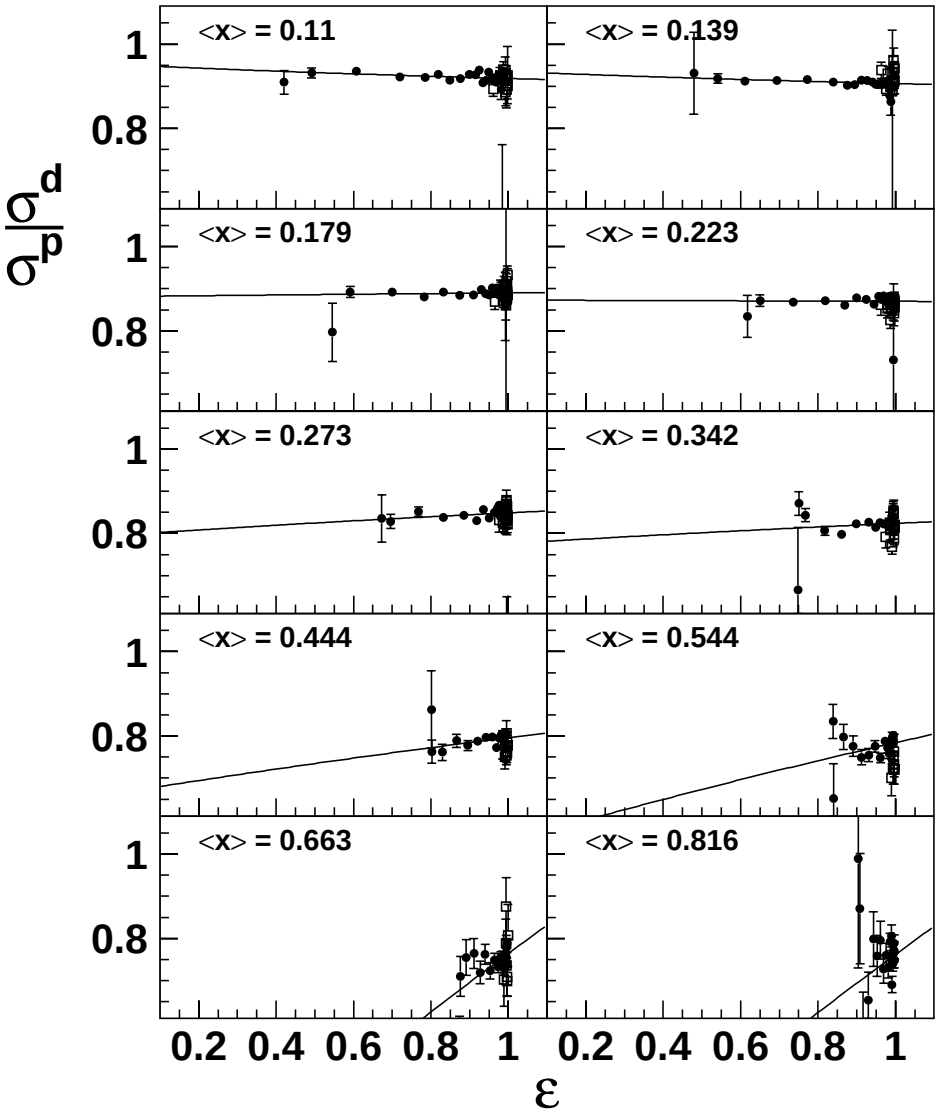

Fig. 4.13: DIS cross-section ratio per nucleon for deuterium to proton as a function of ϵ. Presented are the HERMES data (full circles) and the NMC data (open squares), which were collected at similar Q^2 values. Also shown is the fit as obtained using eq. 4.8.

The second source is the uncertainty on the parameterisation of R. The chosen value of R^p (R1990)[47] directly affects the fit results as can be seen from equation 4.8. To establish the effect of the uncertainty of R^p the fitting procedure was repeated with the value of R plus its uncertainty and R minus its uncertainty. For the region below $Q^2 = 0.35$ GeV^2, where the applicability

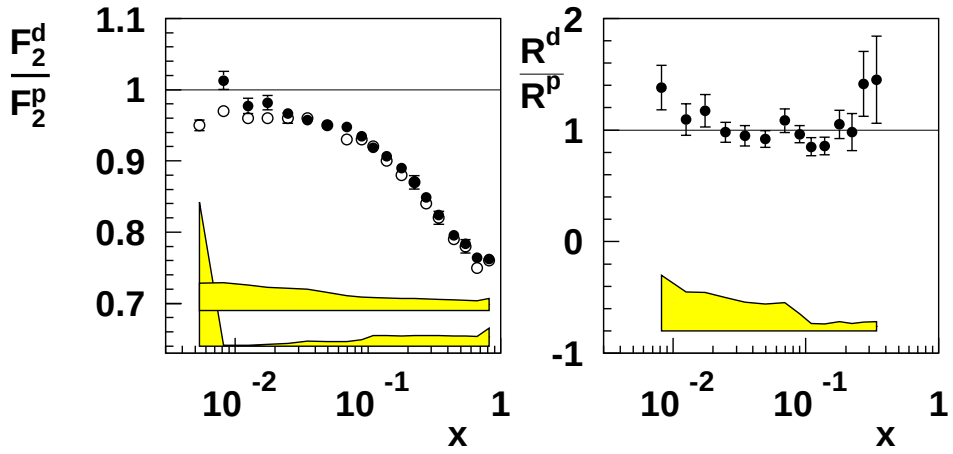

Fig. 4.14: The results from the fit in the ϵ-domain using eq. 4.8. In the left panel the cross-section ratio σ^d/σ^p, as measured directly (open circles), is compared to the extracted structure function ratio F_2^d/F_2^p from the fit in the ϵ domain (solid circles) of the combined HERMES and NMC data. The upper error band indicates the systematic uncertainty on the direct measurement, while the lower band is the result of the uncertainties in the fitting procedure.
In the right panel the extracted ratio R^d/R^p, as obtained from the same fitting procedure, is shown with the error band giving the uncertainties due to the fitting procedure.

of the parameterisations ceases we have used the values as given by the parameterisation anyway, as the errors are large and the effect of changing R^p is found to be minimal. The average of the difference compared to the centre value was taken to be the systematic uncertainty due to the parameterisation of R^p. Both effects were studied separately and added in quadrature as they are independent.

4.6.5 Extraction of $R^d - R^p$ and F_2^d/F_2^p

Existing data on the combination of R^d and R^p are generally presented as the difference $\Delta R = R^d - R^p$. In order to have a direct comparison between the HERMES results and the existing data, ΔR was extracted from the ϵ-dependence of the combined HERMES and NMC data. The fit was carried out using equation 4.9 with ΔR and F_2^d/F_2^p as free parameters. Equation 4.9 can be obtained from 4.8 as an approximation if only the first term in

the Taylor expansion is used:

$$\frac{\sigma^d}{\sigma^p} \simeq \frac{F_2^d}{F_2^p}\left(1 - \frac{1-\epsilon}{(1+R)(1+\epsilon R)}\Delta R\right). \tag{4.9}$$

The extracted values for $\mathrm{F}_2^d/\mathrm{F}_2^p$ from equations 4.8 and 4.9 can be used to check the uncertainty introduced by using only the first term in the Taylor expansion to obtain ΔR. As the extracted values for $\mathrm{F}_2^d/\mathrm{F}_2^p$ are within 0.01% the same as those obtained from the fit using equation 4.8 it can be concluded that the methods are indeed identical and the result of ΔR carries no additional uncertainty. In figure 4.15 the results for ΔR are plotted as a function of Q^2 for different x regions. For comparison the results obtained by NMC and SLAC [1, 2] are shown as well. The systematic uncertainty, as presented by the shaded band, was obtained in the same manner as described in section 4.6.4. It is concluded that in the region of overlap very good agreement is reached with the SLAC and NMC analyses. Moreover, the present analysis provides new data at low x and low Q^2, which also show that $R \simeq 0$.

4.6.6 Extraction of σ_T^d/σ_T^p and σ_L^d/σ_L^p

Apart from showing the result of the present analysis in terms of F_2^d/F_2^p and R^d/R^p (or ΔR), it is also possible to express the results in terms of ratios of longitudinal and transverse photo-absorption cross sections. Therefore, we have rewritten equation 4.8 into the following form:

$$\frac{\sigma^d}{\sigma^p}(\epsilon) = \frac{\sigma_T^d/\sigma_T^p + \epsilon R^p \sigma_L^d/\sigma_L^p}{1+\epsilon R^p} \tag{4.10}$$

The two free parameters in the fit are σ_L^d/σ_L^p and σ_T^d/σ_T^p. This relation allows us to separate the transverse and longitudinal effects on the cross-section ratio. The results from the fit to the combined HERMES and NMC data are shown in figure 4.16. For $\sigma_{\mathrm{L}}^d/\sigma_{\mathrm{L}}^p$ the result is presented in the left panel. The ratio is constant, and close to unity, over the whole x range within the statistical and systematic uncertainties. In the right-hand panel the extracted values of $\sigma_{\mathrm{T}}^d/\sigma_{\mathrm{T}}^p$ are shown. This ratio resembles the behaviour of σ^d/σ^p.

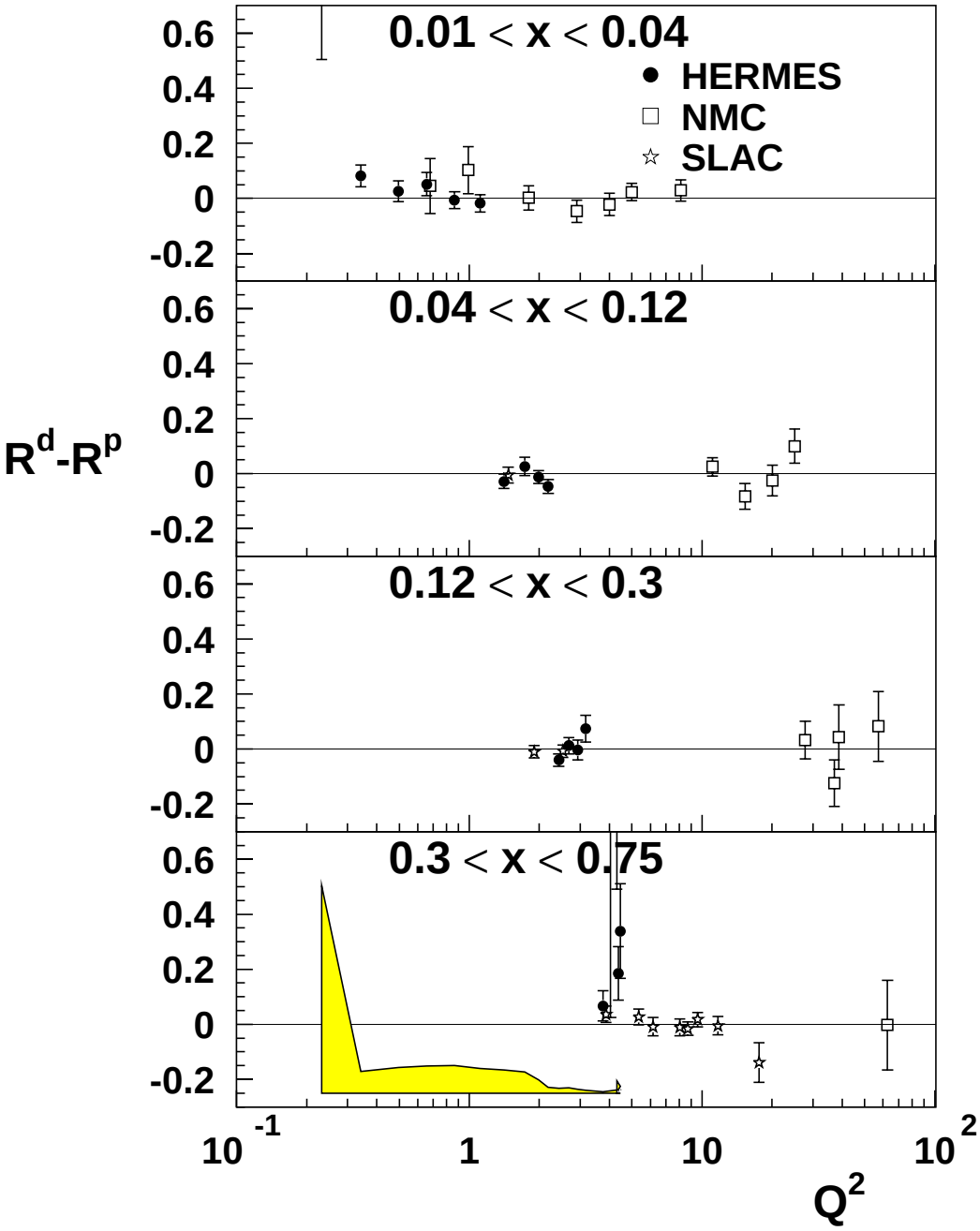

Fig. 4.15: The values of $\Delta R = R^d - R^p$ as a function of Q^2 as obtained by the present analysis of the combined HERMES and NMC data (solid circles) for different x regions compared to the values as obtained by the NMC (open squares) analysis and the SLAC global re-analysis (open stars). The error band indicates the uncertainty due to the fitting procedure.

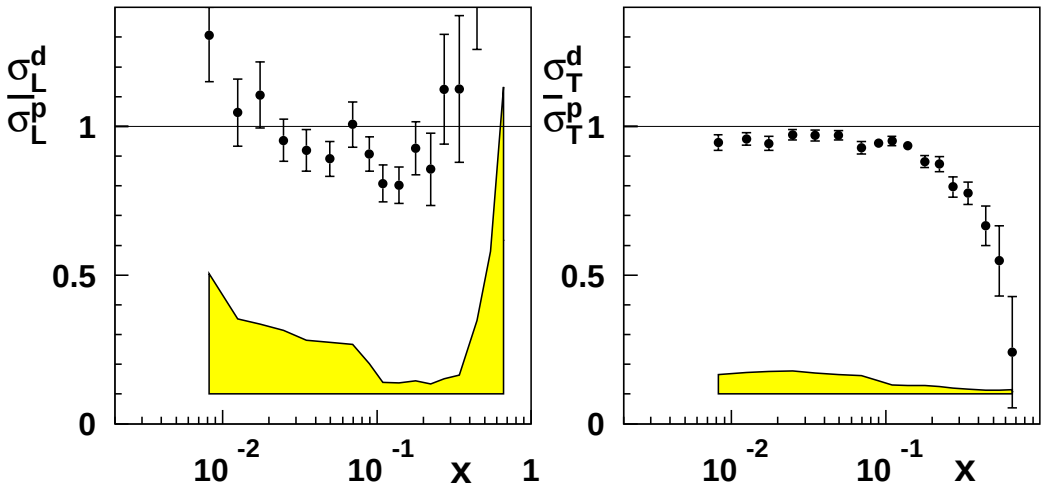

Fig. 4.16: The results of the fits using eq. 4.10. In the left-panel the results for σ_L^d/σ_L^p as a function x are presented, while in the right-hand panel the results for σ_T^d/σ_T^p are shown. The error bands indicate the uncertainties due to the fitting procedure.

4.7 Higher twist effects at high x

The possible flavour dependence of higher twist effects has been investigated at high x, where the valence quarks dominate and the difference between the proton and neutron valence quark content becomes apparent. The latter effect is clearly observed by the large deviation from unity of the cross-section ratio σ^d/σ^p or F_2^n/F_2^p presented in this chapter. At high x nuclear effects and target mass effects play a role as was mentioned in section 2.7. However, since these effects cannot be determined unambiguously, the data analyses do not include a correction for these effects to obtain a model-independent result.

To investigate whether there are higher twist effects one has to compare the experimental data with pQCD calculations performed in Next to Leading Order (NLO). These pQCD calculations are based on Parton Distribution Functions (PDF's) obtained from the fits of the currently available high energy scattering data. There is a continuing effort [48] to fit the currently available data in a QCD framework in order to obtain the most accurate description of the PDF's. These efforts result in precise F_2^d/F_2^p descriptions in leading twist (LT). As an example of this effort we mention the PDF parameterisations obtained by Botje [48]. Since most of the data, on which these parameterisations are based, have been obtained at relatively high Q^2 values,

it is of interest to compare them to the present data which have been collected at relatively low Q^2 values of ~ 2 GeV^2. Such a comparison enables us to investigate whether the leading twist calculations describe the data satisfactorily, or whether possible higher twist effects contribute in certain kinematic regions. For this purpose the ratio F_2^d/F_2^p has been evaluated for both the HERMES and NMC kinematics using the PDF parameterisation of Botje [48]

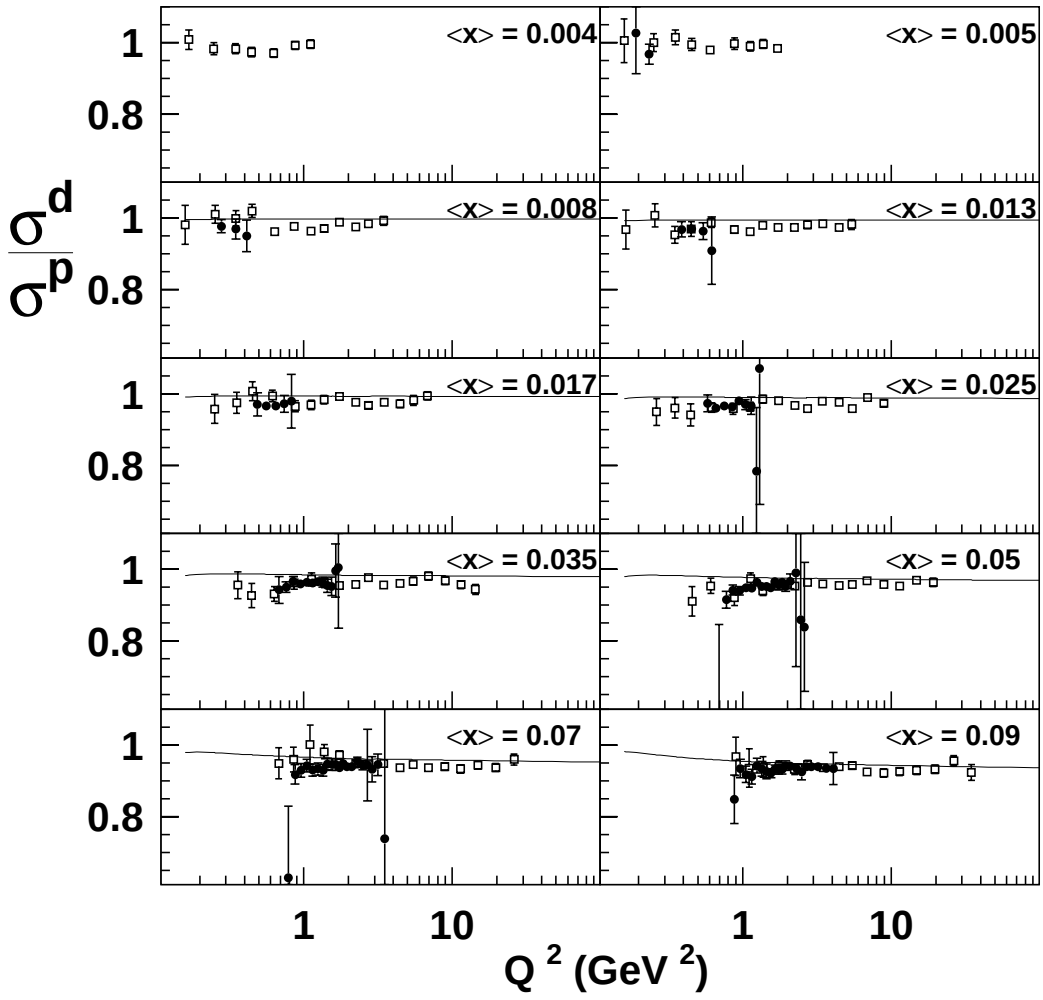

Fig. 4.17: The cross-section ratio per nucleon as a function of Q^2 in the different x regions for the HERMES (full circles), and NMC (open squares) data. Also shown is the prediction for σ^d/σ^p using the latest PDF's in a QCD framework.

In figures 4.17 and 4.18 the calculations are presented together with the

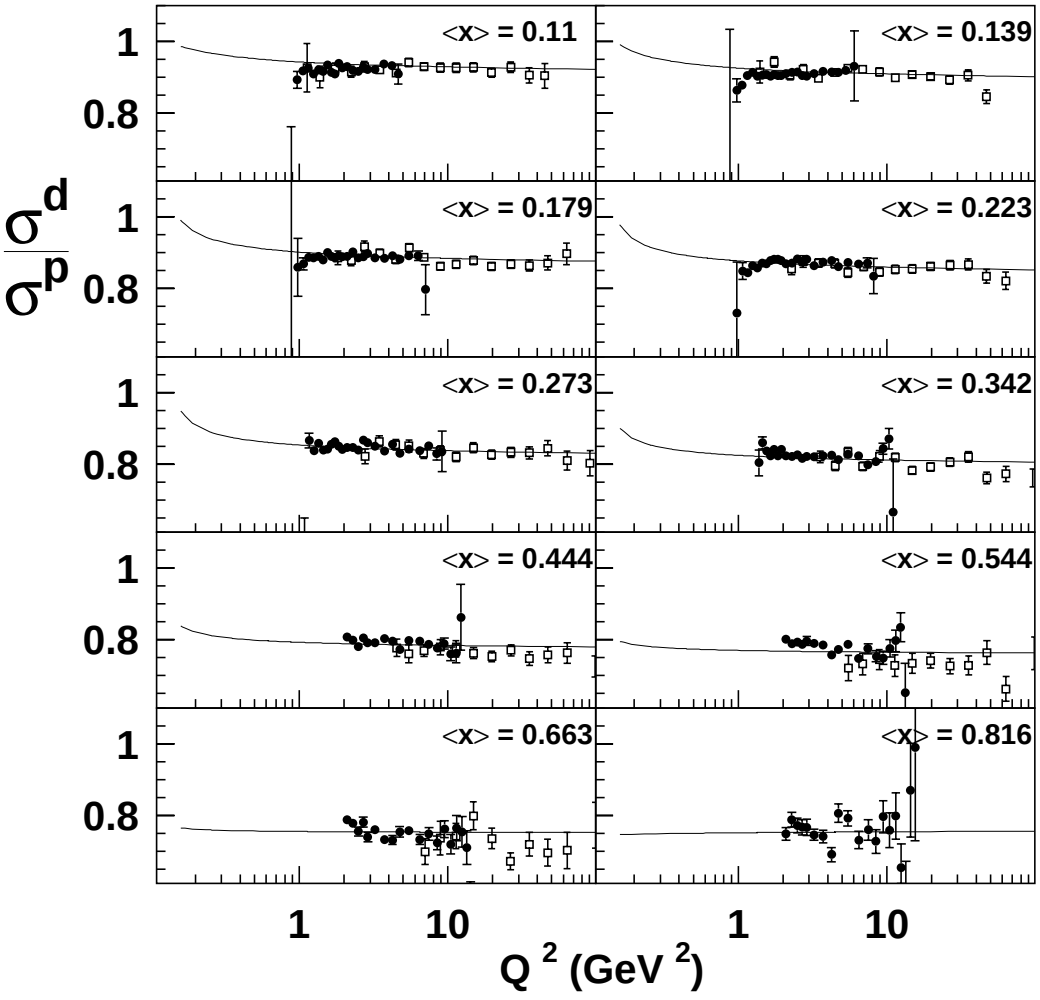

Fig. 4.18: The cross-section ratio per nucleon as a function of Q^2 in the different x regions for the HERMES (full circles), and NMC (open squares) data. Also shown is the prediction for σ^d/σ^p using the latest PDF's in a QCD framework.

HERMES and NMC data versus Q^2 for fixed x-bins. In general, there is a fairly good agreement in all x-bins. In order to search for higher twist effects the following expression is used for $F_2(x, Q^2)$:

$$F_2(x, Q^2) = F_2^{LT}(x, Q^2) \cdot \left(1 + \frac{C(x)}{Q^2}\right), \tag{4.11}$$

with $F_2^{LT}(x, Q^2)$ the leading-twist calculation based on the PDF parameterisation and $C(x)$ the contribution of higher twist terms. As we measure σ^d/σ^p, the following ratio needs to be evaluated:

$$\frac{F_2^n}{F_2^p} = \left(\frac{F_2^n}{F_2^p}\right)^{LT} \cdot \left(1 - \frac{C^p - C^n}{Q^2}\right), \tag{4.12}$$

where F_2^n/F_2^p is calculated directly from σ^d/σ^p because we have found $R^d \simeq R^p$. In this procedure we can only extract higher twist effects which are different for the neutron and the proton. The extracted value of $C^p - C^n$ has been obtained by a minimisation procedure comparing the data to the calculated values. The results are presented in figure 4.19. In the left panel results are presented which are obtained using one of the most recent parameterisations for the PDF's [48], while the result shown in the right panel was obtained with the MRSA [49] PDF's as input. A similar result was

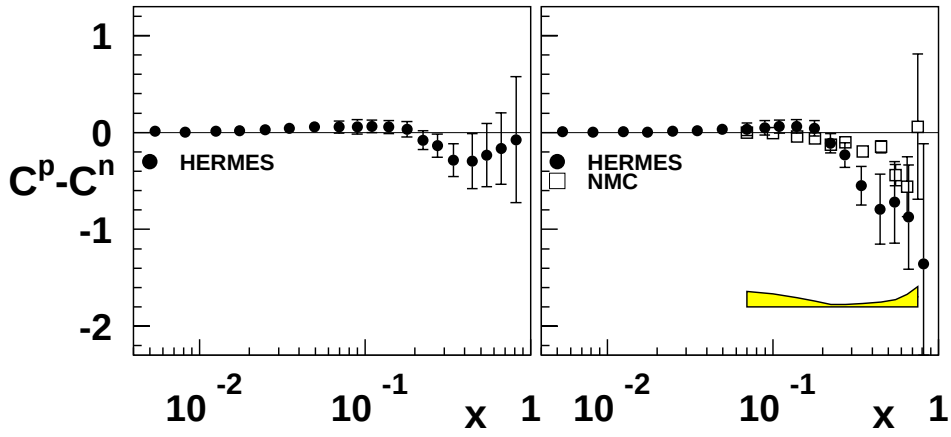

Fig. 4.19: Possible higher twist effects extracted from a comparison between data and QCD predictions. The results shown in the left-hand panel were obtained using the latest PDF's [48]. The results in the right-hand panel were obtained with the older MRSA PDF's as input. Also, the NMC results on $C^p - C^n$ are shown.

obtained by NMC (also using the MRSA PDF's) combining NMC, BCDSM, and SLAC data. The NMC results are plotted in the right panel as well.

For the HERMES data the error bars shown represent both the statistical and sytematical uncertainties as in the fitting procedure these two components cannot be properly separated. The error band shown in the right-hand plot applies to the NMC data. Taking the uncertainties into account the two results shown in the right panel are in qualitative agreement. If the more recent PDF's of Botje are used, a small deviation of $C^p - C^n$ from zero remains, which is, however, barely significant. It is concluded that no unambiguous evidence for flavour-dependent higher twist effects can be found from these data.

4.8 The Gottfried sum rule

In section 2.6 the Gottfried Sum Rule (GSR) was introduced, which relates the difference between the proton and neutron structure functions $F_2^p(x)$ and $F_2^n(x)$ to a possible isospin asymmetry of the sea quarks. The NMC experiment [50] found a significant deviation from 1/3, the value of the GSR expected if $\overline{u}(x) = \overline{d}(x)$. It was concluded that the $\overline{u}$ and $\overline{d}$ contents of the sea are not equal. Here, the first determination of the GSR by the HERMES experiment is presented, based on the measured values of F_2^d/F_2^p and the parameterisation of the world data for F_2^d. As compared to NMC, the GSR value obtained by HERMES is evaluated at a lower Q^2 value, thus enabling the investigation of a possible Q^2 dependence of the GSR. The GSR is defined

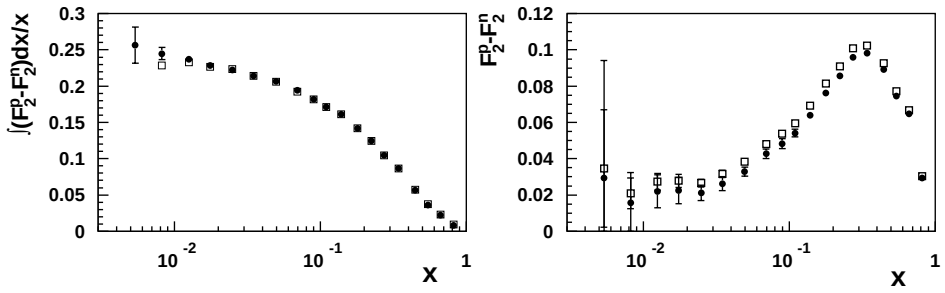

Fig. 4.20: Value of the GSR integral with a running lower limit x_{min} set equal to the x-value of that bin (left panel). The value of $F_2^n - F_2^p$ is shown in the right panel. The NMC data are shown for comparison (open squares).

as:

$$S_{GSR} = \int_0^1 \frac{1}{x}(F_2^p(x) - F_2^n(x))\mathrm{d}x \tag{4.13}$$

and was calculated using the following expression:

$$S_{GSR} = \int_{0.005}^{0.75} 2F_2^d(x) \left(\frac{1 - F_2^d(x)/F_2^p(x)}{F_2^d(x)/F_2^p(x)} \right) \frac{\mathrm{d}x}{x} \tag{4.14}$$

at an average value of Q^2 of 2 GeV^2. The obtained value of the GSR integral is

$$S_{GSR} = 0.256 \pm 0.025 \text{ (stat)} \pm 0.023 \text{ (sys)}.$$

The result is in agreement with the NMC result:

$$S_{GSR}^{NMC} = 0.2281 \pm 0.0065 \text{ (stat)}.$$

To illustrate the evolution of the integral of $F_2^n - F_2^p$ the value of the running integral is shown in the left panel of figure 4.20. At low x the behaviour is rather flat, which indicates that with the extension over the whole x-range towards lower x no significant contribution to the integrand can be expected. At high x the decrease of the difference, $F_2^n - F_2^p$, also reduces the significance of the inclusion of the region up to $x = 1$. Therefore, if the whole x domain would be considered still a deviation from the originally expected value of 1/3 would be obtained. In the right panel of the same figure the difference $F_2^n - F_2^p$ is presented as evaluated in the same way as for the integrand in equation 4.14. A comparison between the results of the present analysis and the NMC data is shown, which shows a good agreement. It is noted that the NMC value was obtained by integrating over x from 0.004 to 0.8. It can be concluded that over a similar range in x, but at an average Q^2 which is a factor of two lower, the deviation from the GSR is essentially the same. Therefore, the difference between the $\overline{u}$ and $\overline{d}$ distributions seems to be the same in the two different Q^2 regions probed by the NMC and HERMES experiments.

4.9 Concluding remarks

The presented analysis has resulted in several results, which have increased the knowledge of the ratio of the structures functions F_2^d and F_2^p. A large number of events was analysed, resulting in a small statistical uncertainty. The systematic uncertainty is of the order of 2%, but somewhat larger at low x mainly due to the uncertainty in the determination of the radiative corrections. Since the HERMES experiment was not designed for studies as discussed in this chapter, the results are surprisingly precise. This enabled a detailed comparison with the precise NMC data obtained at larger average

Q^2 values. The combination with the NMC data made it possible to determine the difference, ΔR, between the ratio of the longitudinal to transverse photo-absorption cross section ratios on the deuteron (R^d) and the proton (R^p). The new data are consistent with zero, which is in agreement with previous results obtained for $\Delta R (= R^d - R^p)$. By studying the Q^2-dependence of F_2^d/F_2^p in comparison with QCD predictions based on recent particle distribution functions an investigation of higher twist effects was performed. A hint for higher twist effects, that are different in the deuteron relative to the proton, was found, but the small size of the effect and the associated margins of uncertainty make it impossible to draw unambiguous conclusions.

The Gottfried Sum Rule was determined over the measured x-domain. A value was obtained similar to the one extracted by NMC, but at an, on average, lower Q^2 value. From the results on F_2^d/F_2^p, as obtained through

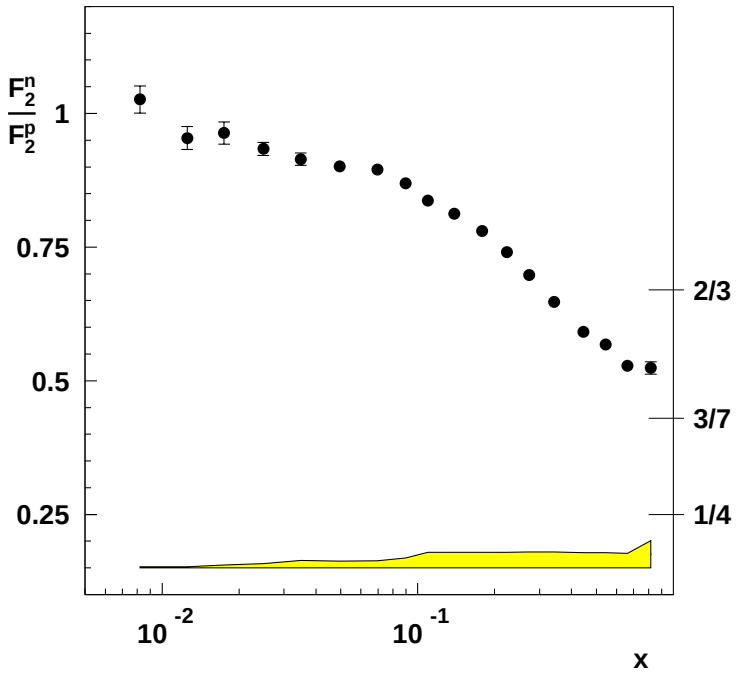

Fig. 4.21: The F_2^n/F_2^p result from the fits in the ϵ-domain compared to the predictions for $x \to 1$ discussed in section 2.7.

fitting the combined HERMES and NMC data, we can directly calculate F_2^n/F_2^p and compare the result to the theoretical predictions presented for high x in section 2.7. In figure 4.21 the results for F_2^n/F_2^p are presented. It can be seen that the current data yield results for $x \to 1$ that are close to the QCD predictions for F_2^n/F_2^p at $x = 1$, i.e. 3/7 especially if it is realised

that the data possibly need to be corrected for higher-twist effects that would reduce F_2^n/F_2^p. However, as long as no corrections are applied for possible higher twist effects, off-shell effects (of the neutron in deuterium) and other nuclear effects, it is hard to draw definite conclusions. In order to avoid such uncertainties it is desirable to measure the same quantity using the tagging method to extract $F_2^n\rfloor_{tag}/F_2^p$. This subject is discussed in the next chapter.